Bioprinting 28 (2022) e00231

Contents lists available at ScienceDirect

Bioprinting

journal homepage: www.sciencedirect.com/journal/bioprinting

Spatiotemporal T cell dynamics in a 3D bioprinted immunotherapy model

Cameron D. Morley [a], Catherine T. Flores [b], Jeffery A. Drake [b], Ginger L. Moore [b], Duane A. Mitchell [b], Thomas E. Angelini [a,c,d,*]

[a] University of Florida, Herbert Wertheim College of Engineering, Department of Mechanical and Aerospace Engineering, Gainesville, FL, 32611, USA
[b] University of Florida Brain Tumor Immunotherapy Program, Preston A. Wells, Jr. Center for Brain Tumor Therapy, Lillian S. Wells Department of Neurosurgery, University of Florida, 1149S Newell Dr, L2-100, Gainesville, FL, 32611, USA
[c] University of Florida, Herbert Wertheim College of Engineering, Department of Materials Science and Engineering, Gainesville, FL, 32611, USA
[d] University of Florida, Herbert Wertheim College of Engineering, J. Crayton Pruitt Family Department of Biomedical Engineering, Gainesville, FL, 32611, USA

ARTICLE INFO

Keywords:
Bioprinting
Cell migration
Adoptive Cell Transfer (ACT)
Microgel

ABSTRACT

3D bioprinting-focused research is often driven by the aspiration to manufacture functional tissues and organs for implantation, yet decades of additional research is likely needed to develop such technologies, broadly. By contrast, we currently have 3D bioprinting tools capable of generating precise, spatially defined distributions of different cell types that can be used in fundamental and applied research, without delay. Here, we demonstrate this capability by 3D printing adoptive immunotherapy models using KR158B cells (murine glioma), hematopoietic stem cells (HSCs), and tumor-reactive T cells. We leverage a recently developed material made from packed microgel particles that serves simultaneously as a 3D printing support material and a 3D culture medium. With this approach we create well-defined 3D cell distributions and investigate the interactions between the different cell populations with time-lapse confocal microscopy. We find that 3D printed tumor spheroids containing HSCs recruit T cells more rapidly than those lacking HSCs, where T cell motion appears to be guided by diffusing cytokines originating at the tumor spheroid surface. After the T cells interact with the glioma structures, we collect the different cell populations by running our 3D bioprinter in reverse and perform transcriptomic analysis. We find that the differences in gene expression, comparing tumor spheroids printed with and without HSCs, are consistent with those found in a murine model. These results establish a path forward for developing validated 3D printed models for pre-clinical testing.

1. Introduction

A long standing and dominant goal in 3D bioprinting research is to manufacture functional tissues and organs [1–9], yet the challenges associated with 3D printing human-scale tissues and organs for implantation indicate that this goal may take many years or decades to achieve in broad applications [8]. By contrast, we can currently generate precise, spatially defined distributions of different cell types using 3D bioprinters to perform fundamental and applied research in new ways that may accelerate progress towards generating functional tissues [2,6,7,10], contributing to efforts in regenerative medicine, pharmacology, and immunology [4,11,12]. For example, the tools and materials of 3D bioprinting could be used to create structures made from tumorigenic, immune, and progenitor cell populations in cancer immunotherapy research on high grade gliomas, where the effectiveness of immunotherapeutic strategies hinges on spatiotemporal cell-cell interactions. In an immunotherapy technique called adoptive cellular therapy (ACT), tumor-reactive T lymphocytes are activated *in vitro* and reintroduced to the host *in vivo* [13–15]. We have demonstrated that the effectiveness of ACT depends on host conditioning and can be markedly enhanced by the co-transfer of bone-marrow derived lineage negative hematopoietic stem cells (HSCs) [16–18]. This adoptive immunotherapeutic strategy has been successful in both human and murine systems [14,15]. However, while murine models provide complete physiological systems for testing treatments, identifying the detailed mechanisms responsible for this efficacy remains challenging because of the limitations of working with mouse models. For example, it is difficult to precisely monitor the motion of adoptively transferred cells toward cancer cell populations due to the challenges associated with imaging intracranial tumors [19–21]. Additionally, precisely controlling the relative

---

[*] Corresponding author. University of Florida, Herbert Wertheim College of Engineering, Department of Mechanical and Aerospace Engineering, Gainesville, FL, 32611, USA.
E-mail address: t.e.angelini@ufl.edu (T.E. Angelini).

https://doi.org/10.1016/j.bprint.2022.e00231
Received 23 April 2022; Received in revised form 18 July 2022; Accepted 25 July 2022

abundances and spatial distributions of the different cells is prohibitive with animal models, impeding systematic exploration of these variables. Thus, an *in vitro* method for creating controlled 3D structures from different cell types directly within a 3D culture environment is needed to enable pre-clinical researchers to interrogate cell-cell interactions and efficiently test new hypotheses. Enabling clinical researchers to structure different cell populations with well-defined 3D spatial relationships to then study their interactions will accelerate progress towards developing new immunotherapeutic strategies.

In the work described in this brief communication, we create spatially structured distributions of the key cell types from a current ACT approach for treating glioma, modifying a recently developed bioprinting and 3D culture method [22,23]. Using a custom-made 3D bioprinter (Fig. S1), we carefully deposit cells into a packed continuum of microscopic hydrogel particles swollen in cell growth media. This pack of microgels provides mechanical support and nutrient reserves for 3D printed cell populations with highly controlled spatial distributions. With this approach, we generate cell distributions having well-defined spatial relationships using KR158B (murine glioma), HSCs, and tumor-reactive T cells to observe T cell migration during ACT. By running our 3D bioprinter in reverse, we collect the different cell populations after the T cells have interacted with the glioma structures for assaying. We find that the transcriptomic changes occurring when tumor spheroids are printed with HSCs are consistent with those found in the murine model. With time-lapse imaging, we see that 3D printed tumor spheroids containing HSCs recruit T cells more rapidly, with T cell motion apparently guided by diffusing cytokines originating in the spheroid. Taken together, these results form a foundation for developing validated models for pre-clinical testing using 3D bioprinting approaches.

2. Results

2.1. 3D printing an adoptive cell therapy model

ACT is performed with a mouse model by orthotopically implanting KR158B cells into the caudate nucleus of the brain and injecting tumor-specific T cells and HSCs into the tail vein (Fig. 1A) [13,16]. We previously demonstrated an ACT platform that employs *in vitro* activated tumor-specific T cells that efficiently target intracranial gliomas [14–18]. These studies showed that in preclinical orthotopic murine models of KR158B glioma, HSC co-transfer significantly enhances the efficacy of ACT using tumor-specific T cells [14–18]. Additionally, HSCs were shown to preferentially migrate to the tumor site and recruit tumor-specific T cells [18]. Since observing and controlling the spatio-temporal interactions between these three cell types in real time is prohibitive in the mouse, here we 3D print structures made from these cell populations into a 3D culture medium made from packed microgels where we can monitor their interactions from the moment the tumor-specific immune cells are delivered (Fig. 1B). We image the printing process by mounting a printer atop an epifluorescence microscope (Fig. 1C), depositing a KR158B spheroid (green) surrounded by a ring of tumor-specific T cells (red). While printing the T cell ring with precise spatial control, the tumor deforms slightly (Movie S1). We explore different spatial relationships by creating T cell rings having diameters between 1.0 mm and 2.5 mm, monitoring how the immune cells that first contact the tumor send molecular signals to the bulk tumor-specific immune cell population (Movie S2). After printing, we image the sample with confocal microscopy to generate 3D renderings of the cell populations (Fig. 1D).

Supplementary video related to this article can be found at https://doi.org/10.1016/j.bprint.2022.e00231

Our previous work showed that activated T cells exhibit ameboid-

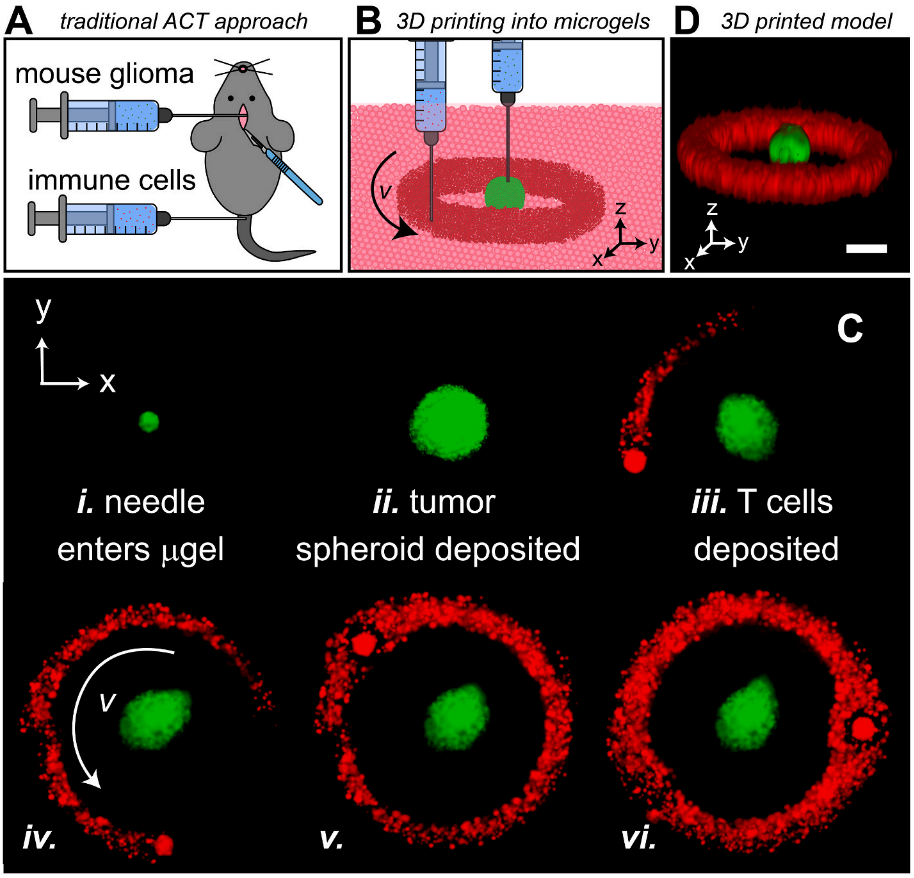

Fig. 1. 3D printed adoptive immunotherapy model. Green cells = KR158B labeled with CMFDA cell tracker green. Red cells = DS red T cells. (A) The mouse model was previously used to develop adoptive cellular therapy (ACT) for treating intracranial glioma, where glioma was implanted in the brain, and antigen specific T cells and hematopoietic stem cells (HSCs) were injected into the tail. (B) We create an *in vitro* model of ACT by 3D printing these three cell types into a medium made from jammed granular microgels, providing versatility in assaying and microscopic imaging. This approach allows spatial relationships between the cell populations to be controlled; interactions can be monitored using fluorescence microscopy. (C) By mounting a 3D printer atop an epifluorescence microscope, we visualize the printing process. (D) 3D laser scanning confocal microscopy measurements are collected to visualize the 3D structure of the model. Scale bar = 500 μm. (For interpretation of the references to colour in this figure legend, the reader is referred to the Web version of this article.)

like migration through the microgel medium used here [24], so we expected the tumor-specific T cells would migrate and reach the spheroids (Fig. 2A). To monitor T cell migration in real-time, we perform time-lapse confocal microscopy. A maximum intensity time-projection shows the T cell population migrating away from the printed location, with some T cells reaching the surface of the tumor within 7 h (Fig. 2B, Movie S2). To confirm this response is due to the presence of the tumor spheroid, we perform control experiments with non-tumor-specific T cells that are reactive against non-tumoroid associated antigen, ovalbumin (OVA). In this case, the non-tumor specific cells do not migrate like their tumor-specific counterparts; migration is suppressed and the non-tumor specific cells do not reach the surface of the spheroid. Likewise, no migration is seen in control experiments with T cells not activated with IL-2 prior to printing (Fig. 2C).

2.2. *Harvesting cell populations for transcriptomic analysis*

Our previous results demonstrated that in orthotopic KR158B glioma-bearing mice, the presence of HSCs at the tumor site was associated with increased accumulation of tumor-reactive T cells [18]. To determine whether the same accumulation occurs in our 3D bioprinted tumor models containing HSCs, we print spheroids made from mixtures of KR158B glioma cells and HSCs, comparing them to spheroids containing only KR158B cells. The tumor spheroid-reactive T cells are then printed in rings around the tumors. After 12 h, we use our 3D printer to harvest the T cells and the model tumors from the microgel medium; with our printer mounted on an inverted microscope, we precisely position the printing nozzle, run the printing code in reverse, aspirating the targeted population. Small deformations of the spheroids are seen as we aspirate the T cells, as occurs while printing (Fig. 3A, Movie S3).

Supplementary video related to this article can be found at https://doi.org/10.1016/j.bprint.2022.e00231

The aspirated cells are prepared for transcriptomic analysis, where we examine the relative gene expression changes induced by the tumor spheroid-reactive T cells in the two spheroid groups using polymerase chain reaction (PCR) (See Methods). Briefly, the extracted KR158B spheroids, with or without HSCs, are immediately lysed and processed for RT2 Profiler PCR Array for T and B Cell Activation. The gene expression profiles evaluated T cell activation markers within the spheroids. Analysis reveals that the spheroids with HSCs have greater than 2-fold increased levels of markers associated with T cell activation including TNFα, CTLA-4, PD-L1 (CD274), as well as chemokine receptors CCR1, CCR2, CCR5 (red datapoints falling outside of solid black lines in Fig. 3B). Likewise, spheroids with HSCs have greater than 2-fold decreased levels of markers associated with tumor progression and immune escape including IDO1 and PD-1 (green datapoints falling outside of solid black lines in Fig. 3B). Similarly, we observe downregulation of CCL28 which has been identified as pro-tumoral in other cancers [25, 26]. These results indicate that the presence of HSCs within the KR158B spheroid leads to increased tumor-reactive T cell migration as previously found in murine models [18]. These results also indicate that the presence of HSCs is associated with greater T cell activation at the spheroid site, which corroborates our previous findings in murine models [16]. These data are a critical first step in validating that 3D printed models, using the approaches described here, can reproduce biological mechanisms found in murine tumor models.

2.3. *Spatiotemporal T cell dynamics*

While transcriptomic analysis indicates that the presence of HSCs increases tumor-reactive T cell migration, these results only indirectly reflect migratory changes. To leverage the advantages of our 3D bioprinting approach, we analyze time-lapse confocal microscopy data to quantify spatiotemporal T cell migration patterns. To create radial fluorescence intensity maps, we calculate azimuthally averaged intensity profiles of the red fluorescence coming from the T cells. We find that a Gaussian line-shape describes these intensity profiles of the T cell rings immediately after printing, and we use the peak location as a reference point for analyzing T cell migration away from the printed location (Fig. 4A). As time progresses, immune cells migrate away from the printed rings, producing exponential tails of fluorescence intensity around the central Gaussian peaks, described by

$$I(R) = I_0 e^{-R/K},$$

where R is the radial distance from the initial T cell ring and K is the characteristic migration distance of the immune cells from their printed location (Fig. 4A and B). We determine K at each time-point by fitting this model to each fluorescence intensity profile. With this approach we compare T cell migration inside the ring, toward the spheroid, to migration outside the ring, away from the spheroid. In both cases, K increases with time, scaling like a piece-wise power law, t^p, where t is time and p appears to change between different regimes of motion. Shortly after printing the ring, the T cells begin to move diffusively, where K scales approximately like $t^{1/2}$. At intermediate times, the cells exhibit super-diffusive motion, where $p > 1/2$. This super-diffusive regime is consistent with Levy-walk motion [27], which T cells have been shown to exhibit previously [28]. At later times, the cells located

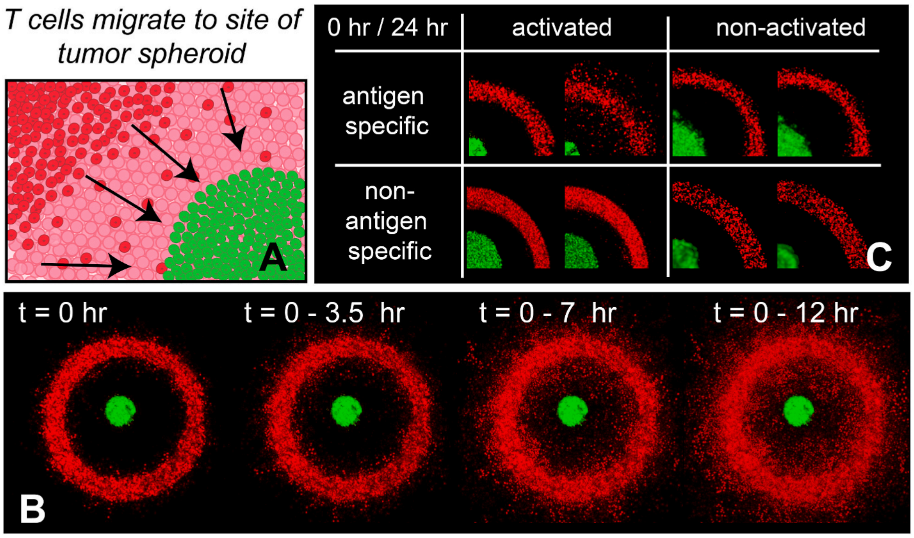

Fig. 2. T cell migration from the printed ring. Green cells = KR158B labeled with CMFDA cell tracker green. Red cells = DS red T cells. (A) We expect the tumor-reactive T cells to migrate toward the site of the tumor and signal the bulk population to generate a collective immune response. (B) Maximum intensity and time projections show the migration patterns of the T cells. (C) Non-activated cells do not migrate from the ring and non-antigen specific cells show minimal migratory behavior from the printed ring. (For interpretation of the references to colour in this figure legend, the reader is referred to the Web version of this article.)

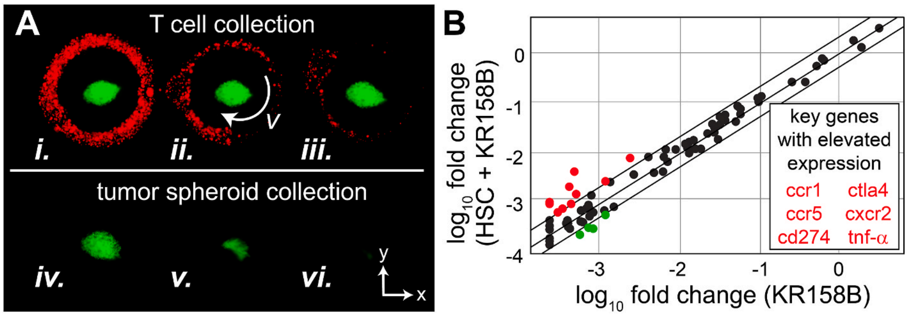

Fig. 3. Retrieval of 3D printed adoptive immunotherapy model for transcriptomic analysis. Green cells = KR158B labeled with CMFDA cell tracker green. Red cells = DS red T cells. (A) By running the printer in reverse and following the same trajectory used to print the structures, we can harvest the T cells (*i., ii., iii.*) and the tumor spheroids separately (*iv., v., vi.*). (B) We retrieve the tumor spheroids, with and without HSCs, separate the cells from any collected microgels, and perform PCR. We find increased expression levels of key genes, such as TNF-a, CTLA-4, and PD-L1, in spheroids containing HSCs. (Genes having greater or less than 2-fold levels of expression relative to housekeeping genes lay outside of the solid black lines. Red datapoints correspond to elevated expression levels; green datapoints correspond to reduced expression levels.). (For interpretation of the references to colour in this figure legend, the reader is referred to the Web version of this article.)

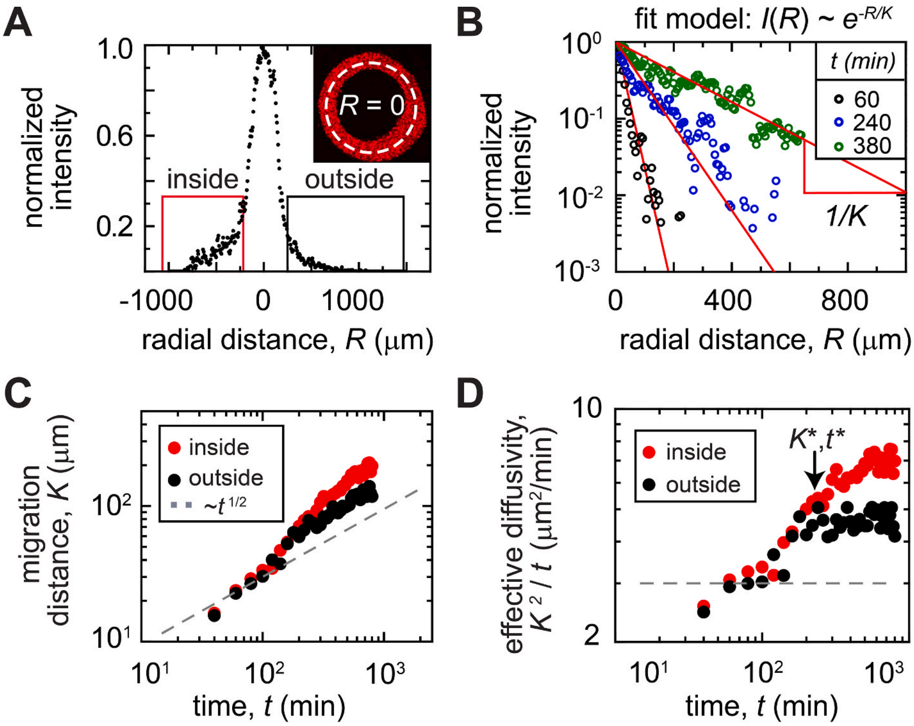

Fig. 4. Quantitative analysis of T cell migration dynamics. Green cells = KR158B labeled with CMFDA cell tracker green. Red cells = DS red T cells. (A) We find that the azimuthally averaged intensity profile of the immune cell ring is well described by a Gaussian line-shape with exponential tails. The exponential tails of fluorescence signal spread outward with increasing time. (B) To determine the T cell migration front location, we fit the tails of the intensity distribution with an exponential function, $I_0e^{-R/K}$, where K is the characteristic T cell migration distance at a given time. (C) Plotting K versus time, we find that the immune cells migrate diffusively at short times and increase to super-diffusive behavior at intermediate times; at later times, the intensity profiles inside and outside the ring begin to diverge, when an inward bias emerges. (D) To identify the time, t^*, and location, K^*, associated with this divergence, we plot an effective diffusivity, K^2/t, versus time. (For interpretation of the references to colour in this figure legend, the reader is referred to the Web version of this article.)

on the inside of the ring, moving inward, migrate more rapidly than the cells on the outside of the ring, moving outward (Fig. 4C).

To see the three regimes of behavior more clearly, we compute an effective diffusivity, given by K^2/t, and plot it versus time (Fig. 4D). A constant effective diffusivity versus time indicates diffusive behavior; for both inwardly and outwardly moving cells, K^2/t exhibits such a plateau at early times. The transition to the third regime of behavior at late time is clearly seen in plots of K^2/t versus time, allowing us to pinpoint a time and distance at which a net-inward bias in migration emerges. To check whether these different regimes of motion could be an artifact of our printing geometry, image processing procedure, or data analysis method, we simulated our experiment using particles moving with perfect Brownian motion (Fig. S2A). We processed the simulated data in the same way as the experimental data, finding qualitatively and quantitatively accurate curves of K versus time, indicating that the regimes of T cell motion we observe are not artifacts (Fig. S2B). We note that in these simulations, inwardly moving cells and outwardly moving cell populations both move diffusively; while the inner and outer concentration profiles will differ in shape and scale, both profiles move diffusively as expected from model cells exhibiting Brownian motion. To test whether these changes in migratory behavior may arise from T cell signaling mediated by the glioma cells, we perform control experiments on T cell rings printed in the absence of tumor spheroids (Fig. S3). In these control experiments we see no significant difference between cells migrating inward and outward at late times while still finding a transition from diffusive to super-diffusive motion at intermediate times.

2.4. Linking T cell motion to cytokine diffusion

Observing the connection between the glioma tumor spheroids and complex T cell migration behavior, we hypothesized that the divergence between inwardly and outwardly directed migration arises from cytokines diffusing from the tumor model surface. To test whether the timescales and length-scales associated with this change in T cell migration are consistent with diffusive molecular signaling, we perform experiments with T cell rings having different diameters; we expected T cells starting from larger diameter rings to exhibit this transition at later times. For the whole population of T cells to sense tumor spheroids that lack HSCs, a “pioneer” T cell must reach the glioma cells and begin secreting cytokines. In each time-lapse video, we visually identify the time-point at which the pioneer T cell makes first contact with the tumor spheroid and record the time, which we call t_1 (Fig. 5B). Treating the time at which inward and outward motion diverge as the characteristic time the population receives the signal, t^*, we compute the diffusion time, $t_d = t^* - t_1$ (Fig. 5C and D). The distance over which the signal diffuses in this time, L_d, can be determined from the location of the migration front at t^*, which we call K^* (Figs. 4D and 5C), and the initial distance between the surface of the T cell ring and the tumor spheroid, d_0 (Fig. 5A). This diffusion distance is given by $L_d = d_0 - K^*$. To account for instances in which two pioneer T cells arrive at similar times but on opposing sides of the tumor, we perform this analysis separately on four quadrants in each time-lapse dataset (Fig. S5). A plot of L_d versus t_d for many different experiments agrees very well with a diffusion law, given by

$$L_d = (6Dt_d)^{1/2},$$

which we fit to the data. We find a molecular diffusion coefficient, $D = 2.5 \times 10^{-8}$ cm^2/s; a small cytokine like IL-2 has a diffusion coefficient of approximately 10^{-7} cm^2/s in water, but can depend on the suspending medium [29,30]. In the jammed microgels used here, we expect molecular diffusion coefficients to be about ¼ their value in water, as we found previously in quantitative molecular diffusion studies [22]. Thus, our results are consistent with T cell signaling through cytokine diffusion. To confirm these results, we performed the same analysis on data from experiments using the HSC loaded tumors, which are expected produce signaling molecules for the entire T cell population from the start of the experiments [16], which sets $t_1 = 0$. Plotting L_d and t_d for these experiments, we find agreement with the data from tumor spheroids lacking HSCs; both sets of experiments are described by the same diffusion law with the same diffusion coefficient, suggesting the HSCs serve as pioneer immune cells, eliminating the delay time required for the immune cells to stochastically move around until they encounter the tumor spheroid (Fig. 5D, S4).

3. Conclusion

In the work presented within this brief communication, we developed a well-controlled and versatile method for studying cell-cell interactions in space and time, creating 3D distributions of different cell types using a combination of 3D bioprinting and a microgel-based support and culture medium. Recently, bioprinting has been used to control spatial relationships between stromal cell and cancer cell populations to investigate the effects of tumor microenvironment on the disease [31–35]. Often, 3D bioprinting approaches involve fabricating a cell-laden scaffold that is later seeded by a second cell population, randomly dispersed throughout large pore-spaces within the scaffold [36,37]. By contrast, our approach does not rely on creating a self-supporting scaffold and enables multiple cell populations to be distributed in space with few restrictions, creating well-controlled initial conditions for experimentation. By avoiding the need to create a self-supporting scaffold or to simultaneously extrude two populations in a structured arrangement [34,36], our approach significantly mitigates the common requirements of specialized 3D printing inks or instrumentation.

Here we also demonstrated that our 3D bioprinting approach can be used to harvest the different cell populations and perform transcriptomic analysis, revealing that the 3D printed glioma tumor spheroids containing HSCs elicit increased tumor-reactive T cell migration as expected from our previous *in vivo* studies [14–18]. Our spatiotemporal analysis of T cell migration shows that this response most likely arises from

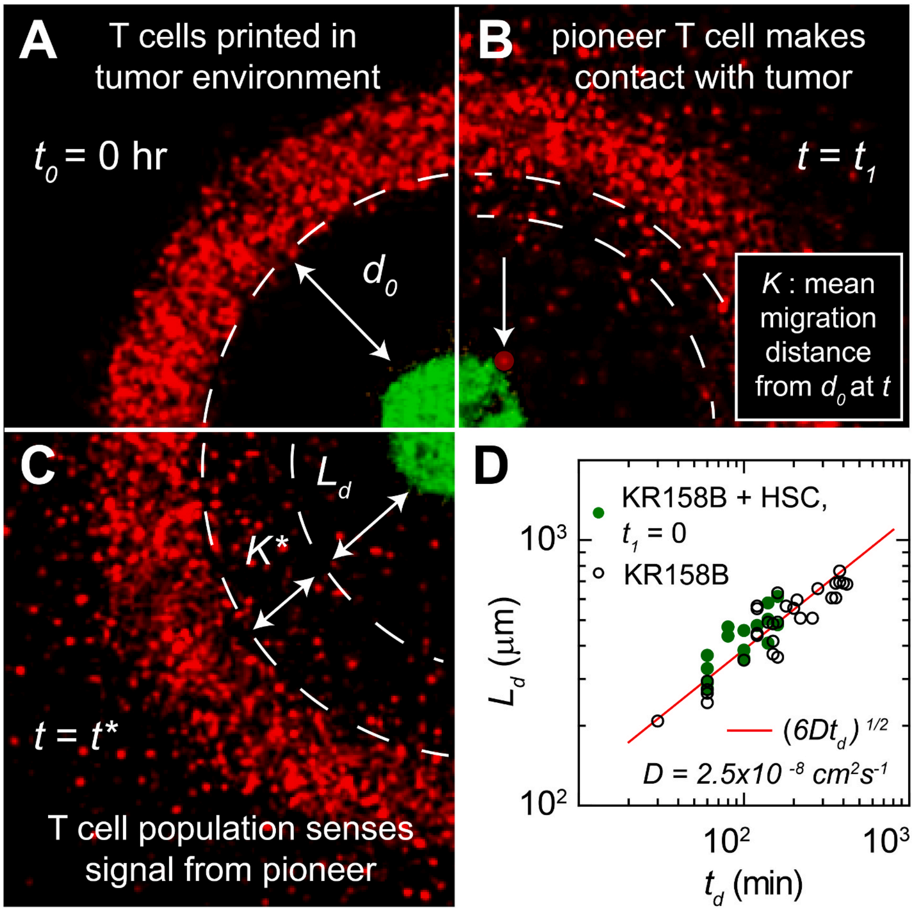

Fig. 5. Establishing the time scales and length scales associated with initiating the T cell response. Green cells = KR158B labeled with CMFDA cell tracker green. Red cells = DS red T cells. (A–D) The time a diffusing signal will travel from the spheroid surface to the T cell population, t_d, is given by t^*- t_1, where t_1 is the time at which the first T cell contacts the tumor. The corresponding diffusion length, L_d, is given by d_0 - K^*, where d_0 is the distance between the T cell ring and the spheroid surface at $t = 0$. (h) We find that $L_d \sim t_d^{\ 1/2}$ and the fitted diffusion coefficient, D, is consistent with that of a cytokine in microgels. We find data from HSC laden spheroids overlay the data from HSC-free spheroid conditions after setting $t_1 = 0$. (For interpretation of the references to colour in this figure legend, the reader is referred to the Web version of this article.)

diffusive molecular signaling, in which T cell migration becomes biased toward the tumor spheroids after a delay time that is apparently controlled by a molecular diffusion coefficient and the proximity between the T cell population and the tumor spheroid. Before this change in migration occurs, we observe two additional regimes of T cell migration: diffusive motion at the earliest times and super-diffusive motion at intermediate times. We were surprised to find that these regimes of T cell migration did not require the presence of a tumor spheroid. Recent work on quorum sensing in the immune system has shown that the secretion and sensing of autoinducers enable individual T cells to measure the number density of the T cell population in which they reside, feeding back to control how they migrate [38]. For example, IL-2 acts as an autoinducer in CD4$^+$ T cell populations [39,40]. Additionally, CD8$^+$ T cells exhibit quorum sensing capabilities, though the detailed mechanism is still being investigated [41]. Approximately 80–90% of T cell population used in our study are CD8$^+$, so it is possible that the early transition we observe in T cell migration results from a quorum sensing mechanism, dependent on T cell density without requiring the presence of a tumor spheroid. We envision that in future work, the quorum sensing hypothesis can be investigated in great detail and with a high degree of control, using the approach described here. By tracking individual cells, the spatially heterogeneous cell density can be measured and correlated with changes in T cell migration. By embedding functionalized enzyme-linked immunofluorescence assay (ELISA) beads in the microgel medium, spatiotemporal concentration gradients of cytokines could be measured to link quorum sensing directly to autoinducer profiles [42].

While the work reported here highlights the ability to perform detailed studies of ACT in a glioma model, the method can be generalized to create *in vitro* models for studying interactions between immune cells and different tissues. In many areas of immunological research, tissue cells are co-cultured with immune cells; T cells are co-cultured with primary pancreatic islets in Type 1 diabetes research, with tumor cells in cancer research, and with explanted tissue in vaccine research [12,43–47]. Such approaches have been used recently in research on SARS-CoV-2 [43]. Employing the methods described here in this diversity of areas would enable experiments to be designed in ways that were previously exceedingly difficult or impossible; embedding or dispersing multiple cell types, tissue explants, spheroids, or organoids in ECM or engineered scaffolding is extremely challenging to do with precision. Moreover, embedding these components in matrices or scaffolds creates challenges with harvesting selected components for targeted assaying. By contrast, the approach described here enables components of *in vitro* models to be added or harvested at practically any place or time. Additionally, solutions of antibodies, pharmaceuticals, or therapeutic reagents can be deposited in the same way that cell populations are printed. While the versatility of our method is matched by the existing tools of traditional 2D culture, the importance of working in 3D is becoming widely accepted [48–50]. Thus, with further validation in different cell and tissue systems, we believe the method described here for creating and studying *in vitro* models will enable a diversity of researchers to design experiments on cell-cell interactions in 3D with few restrictions.

4. Materials and methods

4.1. Cell culture

As described previously [16], cells were harvested from female 6- to 8-week-old C57BL/6 mice (Jackson Laboratories stock 000664) and transgenic DsRed mice (Jackson Laboratories stock 006051) for experiments. The investigators adhered to the “Guide for the Care and Use of Laboratory Animals” as proposed by the committee on care of Laboratory Animal Resources Commission on Life Sciences, National Research Council. The facilities at the University of Florida Animal Care Services are fully accredited by the American Association for Accreditation of Laboratory Animal Care, and all studies were approved by the University of Florida Institutional Animal Care and Use Committee.

HSCs are isolated from the bone marrow of female 6- to 8-week-old C57/BL6 mice according to a previous report [16]. Briefly, mononuclear cells (MNCs) are collected after lysing the red blood cells. Lineage negative (Lin-) cells are isolated using the magnetic bead isolation kit (Miltenyi Biotec, cat. 130-090-858). MNCs are incubated with Biotin−Antibody Cocktail (10 μl per 10^7 total cells) at 37 °C and 5% CO_2 for 10 min, followed by incubation with Anti-Biotin MicroBeads (20 μl per 10^7 total cells). The mixture is then washed in PBS, resuspended in buffer and placed through a magnetic separation column for separate Lin-cells. The Lin-population is then labeled with either anti-Sca-1-biotin (10 μL per 10^7 MNC, Miltenyi cat. 130-101-885), CD117 MicroBeads (20 μL per 10^7 MNC, Miltenyi cat. 130-091-224), anti-Prominin-1-biotin (5 μL per 10^6 MNC, Miltenyi cat. 130-101-851), anti-CD38-biotin (5 μL per 10^6 MNC, Miltenyi cat. 130-109-253), or anti-CCR2−biotin (5 μL per 10^6 MNC, Miltenyi cat. 130-108-721), incubated for 10 min at 4 °C, then 20 μL of anti-biotin microbead was added per 10^7 MNC, and incubated for 15 min at 4 °C in order to further isolate the Lin- HSCs to stem cell subsets. This mixture is then washed with PBS and centrifuged at $500\times g$ for 5 min, where cells are resuspended in 500 μL buffer per 10^8 MNC and placed through magnetic column.

Tumor-reactive T cells are isolated from the spleen of transgenic DsRed mice. To prime the T cells for the tumor-specific neo-antigens, the bone marrow is extracted from the mice, red blood cells are lysed, and the resulting MNCs population is cultured in GM-CSF (10 ng/mL, R&D, cat. 415-ML/CF) and IL-4 (10 ng/mL, R&D, cat. 404-ML/CF) for 9 days. Dendritic cells (DCs) are then electroporated with 25 μg total RNA isolated from tumor tissue. Naïve mice are primed with 2.5×10^5 total tumor RNA-pulsed dendritic cells. After one week, splenocytes are harvested and co-cultured *ex vivo* using total tumor RNA-pulsed dendritic cells and IL-2 (50 U/mL, R&D, cat. 402−ML/CF) for 5 days.

4.2. Microgel fabrication and material property characterization

We synthesize the microgels used here following a method described in previous work [23]. Briefly, a solution of acrylamide monomer (8% w/w), methacrylic acid comonomer (2% w/w), poly(ethylene glycol) diacrylate (1% w/w, MW = 700 g mol^{-1}), and azobisisobutyronitrile (0.1% w/w) is prepared in 490 mL of ethanol. Polymerizing networks grow until they reach a critical size and become insoluble, generating a white precipitate. When polymerization is complete, the precipitate is collected, filtered to remove potential residual monomer, and dried in an oven to yield a loose white powder. The purified microgel powder is mixed with cell growth media at a concentration of 2.2% (w/w) and dispersed in a centrifugal speed mixer at 3500 rpm in 5-min intervals until all aggregates are disrupted. The microgel is then neutralized to a pH of 7.4 with NaOH and 25 mM HEPES buffer (Fisher Sci., cat. BP299-100), then left to swell overnight, producing the microgel 3D printing and growth media.

Similarly, we quantify the mechanical properties and yielding behavior of the microgels using a method described in previous work [23]. In the previously published work, we found that performing oscillatory rheology on the 2.2% (w/w) microgel pack reveals a weakly frequency dependent storage modulus, G', that is greater than the loss modulus, G'', across five decades of frequency. Performing unidirectional shear rheology on the pack of microgels, we find they behave as a Herschel-Bulkley yield stress fluid. Taken collectively, these rheological properties facilitate our ability to precisely establish spatial relationships between multiple cell populations and support those 3D printed constructs over long timescales.

4.3. Bioprinting preparations

To create the 3D printed tumor spheroids, we first culture KR158B cells (murine glioma) in Dulbecco's Modified Eagle Medium (DMEM) with 4.5 g/L glucose, L-glutamine, and sodium pyruvate supplemented with 10% FBS and 1% penicillin streptomycin on coated polystyrene dishes. Similar to the protocol developed previously [23], the KR158B cells are dyed with cell tracker green (CMFDA) once they have reached 70% confluence. We harvest the cells by washing with PBS and incubating in 3 mL of 5% Trypsin-EDTA solution for 5 min. The cells are removed from the dish and placed into a 15 mL centrifuge tube, where they are centrifuged at 160 × *g* for 1 min. The supernatant is removed from the tube and bovine collagen-1 (Advanced Biomatrix cat. 5010-50 ML) solution is added to achieve a final collagen-1 concentration of 1.0 mg mL^{-1}. The cell pellet is dispersed with gentle pipette mixing and loaded into a 100 μL Hamilton gas-tight syringe. A sterile, blunt-tip 30-gauge luer-lock needle is affixed to the syringe, which is then mounted onto the printer. Tumor spheroids are generated by submerging the needle tip into the packed microgel support medium and extruding 15 nL of the cell-collagen mixture. HSC loaded tumor spheroids are generated by mixing in KR158B cells at a 1:1 cell ratio just before adding collagen-1.

T cell printing preparations are similar to those for printing tumor spheroids; we harvest the T cells from the polystyrene dish and load them into the syringe. T cells are not printed with extracellular matrix, however. Instead, we dilute the T cells to a density of approximately 50% (v/v) by mixing with microgels (Fig. S6). Within a T cell preparation, we have used cell counts between 1 and 25 M cells, which was determined with a hemocytometer, depending on the specific experiment; fewer cells were required to print the microscopy experiments than those intended for PCR. Further, we do not observe cell death from pipette mixing during preparation. This process prevents the T cells from settling in the syringe throughout the printing process. In this way, we maintain a constant cell density from well-to-well and across the different experimental conditions like tumor spheroid compositions and T cell ring radius. For time-lapse microscopy experiments, we load 1.5 mL of microgel media into each well of a 12-well, glass bottomed, opaque walled plate. These plates are incubated at 37 °C and 5% CO_2 for 1–2 h before transferring to our printer, where rings of differing diameters are then printed into the wells.

In experiments where we probe changes in gene expression between two different tumor spheroid conditions, where detection requires large cell populations, we print 30 replicates of each tumor composition into single wells of a 96 well, glass bottom dish loaded with 100 μL of microgel media. Each tumor spheroid is surrounded by a 2.0 mm diameter T cell ring. Under these conditions, we collect approximately 6×10^5 tumor cells and 2×10^6 T cells per experiment. To extract the T cells from the microgels, we run the T cell loop printing code and pump in reverse. Similarly, we center the needle and run the pump in reverse to extract the tumor spheroids.

4.4. Microgel and cell separation for PCR of tumor spheroids

Each of the 30 tumor spheroid replicates are harvested after 12 h in co-culture and binned into a 0.5 mL Eppendorf tube. After harvesting cells, we perform a wash step to remove microgels collected with the cells prior to performing transcriptomic analysis. We find that the tumor spheroids are robust and remain intact during the collection process. Since they are between 300 and 500 μm in diameter and the microgel particles are between 1 and 10 μm in diameter, we use a 40 μm pore size cell strainer to separate the two materials. To separate T cells from microgels, whose size will be on the order of the microgels, we create a fluid density gradient. The T cell-microgel mixture is pipetted on top of a 25% Glycerol solution. The microgels are 97.8% cell growth media and have a density very close to that of water, while the cells are closer to 1.1–1.3 g/cm^3. After 1 min of centrifugation at 200 × g, the cells pellet at the bottom of the tube and the glycerol and microgels are gently aspirated.

Quality and quantity of RNA was measured using NanoDrop 2000 after the tumor spheroids are isolated from the microgels. Total tumor spheroid RNA isolation from 3D printed KR158B cells was performed with RNeasy mini kit (Qiagen, cat. 74104) as per the manufacturer's protocol. 3D printed tumor spheroids were dissociated and analyzed with the RT^2 Profiler Array Cancer Inflammation and Immunity Crosstalk (Qiagen cat. PAMM-181ZD-12) and results are shown as fold change for each tumor spheroid condition relative to the housekeeping genes.

4.5. Time-lapse imaging and analysis

To monitor the migratory patterns of the T cells, we collect 3D stacks of fluorescence images using a Nikon laser scanning confocal microscope with a C2+ scan head and 4x objective with a numerical aperture (NA) of 0.2. Prior to loading the well plate onto the microscope, we add 25 mM Hepes to maintain a pH of 7.4 and incubate the well plate at 37 °C and 5% CO_2. To maintain humidity in the chamber, CO_2 is first pumped through a bubbler and approximately 30 mL of sterile H_2O is added to the interstitial chambers of the well plate. During imaging, the laser is scanned using a pixel dwell time of 4.8 ms and at a power setting such that photobleaching does not occur over the approximately 12-h duration of the experiments. As previously mentioned, we print into 12-well plates with opaque walls to minimize light exposure and image every 30 min with the FITC ($\lambda = 488$ nm) and TRITC ($\lambda = 561$ nm) lasers. Images are collected with a spatial sampling frequency of 6.21 μm per pixel in the 512 x 512-pixel X–Y plane and 25 μm per step in the Z direction, where each Z-stack consists of 25–30 images on average.

Due to the printed geometry, we find that the vast majority of T cell migration comes in the X–Y direction, thus the resolution in the Z plane is negligible when examining migratory patterns. For similar reasons, we perform the intensity analysis on maximum intensity projections of the confocal Z-stacks. To remove random noise, the images are blurred with a Gaussian kernel having a half-width of 0.7 pixels. To amplify the detectable signal from single T cells above the noise threshold, we take the logarithm of each image. To correct for photobleaching that may occur during the experiment, we normalize each image in the time-stack by the average intensity of the first image before performing the spatial intensity analysis shown in Fig. 4.

CRediT authorship contribution statement

Cameron D. Morley: Formal analysis, Writing – original draft, conceived, designed, and executed . **Catherine T. Flores:** , and wrote the paper, Formal analysis, helped perform transcriptomic analysis of extracted tumor spheroids, provided the engineered T cells and contributed important biological knowledge. **Jeffery A. Drake:** Formal analysis, helped perform transcriptomic analysis of extracted tumor spheroids. **Ginger L. Moore:** provided the engineered T cells and contributed important biological knowledge. **Duane A. Mitchell:** Writing – review & editing, assisted with writing and editing the paper. **Thomas E. Angelini:** analyzed the data, , Formal analysis, Writing – original draft, conceived the experiment, developed the particle diffusion simulation, analyzed the data, and wrote the paper.

Declaration of competing interest

The authors declare that they have no known competing financial interests or personal relationships that could have appeared to influence the work reported in this paper.

Data availability

Data will be made available on request.

Acknowledgments

The authors thank Anton Paar for the use of the Anton Paar 702 rheometer through their VIP academic research program. The authors would also like to thank DEKA for designing and fabricating a lightweight and modular 3D bioprinter that made microscopy enabled printing possible. We would also like to thank Bayli DiVita, Brandon Wummer, and Carmelle Kuizon for assisting with HSC harvesting. Research reported in this publication was supported by the National Institutes of Health under the National Institute of Neurological Disorders and Stroke award R01NS112315 (PI: Flores, Co–I: Angelini) and National Cancer Institute award R01CA195563.

Appendix A. Supplementary data

Supplementary data to this article can be found online at https://doi.org/10.1016/j.bprint.2022.e00231.

References

[1] M.A. Heinrich, et al., 3D bioprinting: from benches to translational applications, Small 15 (23) (2019), 1805510.

[2] A. Lee, et al., 3D bioprinting of collagen to rebuild components of the human heart, Science 365 (6452) (2019) 482–487.

[3] C. Mandrycky, Z. Wang, K. Kim, D.-H. Kim, 3D bioprinting for engineering complex tissues, Biotechnol. Adv. 34 (4) (2016) 422–434.

[4] S.V. Murphy, A. Atala, 3D bioprinting of tissues and organs, Nat. Biotechnol. 32 (8) (2014) 773–785, https://doi.org/10.1038/nbt.2958, 2014/08/01.

[5] C.S. Ong, et al., 3D bioprinting using stem cells, Pediatr. Res. 83 (1) (2018) 223–231.

[6] M.A. Skylar-Scott, et al., Biomanufacturing of organ-specific tissues with high cellular density and embedded vascular channels, Sci. Adv. 5 (9) (2019) eaaw2459.

[7] A.N. Leberfinger, et al., Bioprinting functional tissues, Acta Biomater. 95 (2019) 32–49.

[8] W.L. Ng, C.K. Chua, Y.-F. Shen, Print me an organ! Why we are not there yet, Prog. Polym. Sci. 97 (2019), 101145.

[9] L. Neufeld, et al., Microengineered perfusable 3D-bioprinted glioblastoma model for in vivo mimicry of tumor microenvironment, Sci. Adv. 7 (34) (2021) eabi9119.

[10] B. Grigoryan, et al., Development, characterization, and applications of multi-material stereolithography bioprinting, Sci. Rep. 11 (1) (2021) 1–13.

[11] W. Peng, P. Datta, B. Ayan, V. Ozbolat, D. Sosnoski, I.T. Ozbolat, 3D bioprinting for drug discovery and development in pharmaceutics, Acta Biomater. 57 (2017) 26–46.

[12] M. Tang, et al., Three-dimensional bioprinted glioblastoma microenvironments model cellular dependencies and immune interactions, Cell Res. (2020) 1–21.

[13] S. Rosenberg, Lymphokine-activated killer cells: a new approach to immunotherapy of cancer, JNCI: J. Natl. Cancer Inst. 75 (4) (1985) 595–603, https://doi.org/10.1093/jnci/75.4.595.

[14] C. Flores, et al., Massive clonal expansion of medulloblastoma-specific T cells during adoptive cellular therapy, Sci. Adv. 5 (11) (2019) eaav9879.

[15] T.J. Wildes, et al., Immune escape after adoptive T-cell therapy for malignant gliomas, Clin. Cancer Res. 26 (21) (2020) 5689–5700.

[16] C.T. Flores, et al., Lin−CCR2+ hematopoietic stem and progenitor cells overcome resistance to PD-1 blockade, Nat. Commun. 9 (1) (2018) 4313, https://doi.org/10.1038/s41467-018-06182-5, 2018/10/17.

[17] T.J. Wildes, et al., Cross-talk between T cells and hematopoietic stem cells during adoptive cellular therapy for malignant glioma, Clin. Cancer Res. 24 (16) (2018) 3955–3966.

[18] C. Flores, et al., Novel role of hematopoietic stem cells in immunologic rejection of malignant gliomas, OncoImmunology 4 (3) (2015), e994374.

[19] K. Yamauchi, et al., Real-time in vivo dual-color imaging of intracapillary cancer cell and nucleus deformation and migration, Cancer Res. 65 (10) (2005) 4246–4252.

[20] R.M. Hoffman, M. Yang, Subcellular imaging in the live mouse, Nat. Protoc. 1 (2) (2006) 775.

[21] R.M. Hoffman, The multiple uses of fluorescent proteins to visualize cancer in vivo, Nat. Rev. Cancer 5 (10) (2005) 796–806, https://doi.org/10.1038/nrc1717, 2005/10/01.

[22] T. Bhattacharjee, et al., Liquid-like solids support cells in 3D, ACS Biomater. Sci. Eng. 2 (10) (2016) 1787–1795.

[23] C.D. Morley, et al., Quantitative characterization of 3D bioprinted structural elements under cell generated forces, Nat. Commun. 10 (1) (2019) 3029, https://doi.org/10.1038/s41467-019-10919-1, 2019/07/10.

[24] T. Bhattacharjee, T.E. Angelini, 3D T cell motility in jammed microgels, J. Phys. Appl. Phys. 52 (2) (2018), 024006.

[25] L. Ren, Y. Yu, L. Wang, Z. Zhu, R. Lu, Z. Yao, Hypoxia-induced CCL28 promotes recruitment of regulatory T cells and tumor growth in liver cancer, Oncotarget 7 (46) (2016), 75763.

[26] A. Facciabene, et al., Tumour hypoxia promotes tolerance and angiogenesis via CCL28 and Treg cells, Nature 475 (7355) (2011) 226–230.

[27] G.M. Viswanathan, E. Raposo, M. Da Luz, Lévy flights and superdiffusion in the context of biological encounters and random searches, Phys. Life Rev. 5 (3) (2008) 133–150.

[28] A. Gérard, et al., Detection of rare antigen-presenting cells through T cell-intrinsic meandering motility, mediated by Myo1g, Cell 158 (3) (2014) 492–505.

[29] T. Weidemann, R. Worch, K. Kurgonaite, M. Hintersteiner, C. Bökel, P. Schwille, Single cell analysis of ligand binding and complex formation of interleukin-4 receptor subunits, Biophys. J. 101 (10) (2011) 2360–2369.

[30] C.W. Yung, W.E. Bentley, T.A. Barbari, Diffusion of interleukin-2 from cells overlaid with cytocompatible enzyme-crosslinked gelatin hydrogels, J. Biomed. Mater. Res. 95 (1) (2010) 25–32.

[31] J.A. Belgodere, C.T. King, J.B. Bursavich, M.E. Burow, E.C. Martin, J.P. Jung, Engineering breast cancer microenvironments and 3D bioprinting, Front. Bioeng. Biotechnol. 6 (2018) 66.

[32] S. Knowlton, S. Onal, C.H. Yu, J.J. Zhao, S. Tasoglu, Bioprinting for cancer research, Trends Biotechnol. 33 (9) (2015) 504–513.

[33] E.M. Langer, et al., Modeling tumor phenotypes in vitro with three-dimensional bioprinting, Cell Rep. 26 (3) (2019) 608–623, e6.

[34] J.M. Grolman, D. Zhang, A.M. Smith, J.S. Moore, K.A. Kilian, Rapid 3D extrusion of synthetic tumor microenvironments, Adv. Mater. 27 (37) (2015) 5512–5517.

[35] Y.S. Zhang, M. Duchamp, R. Oklu, L.W. Ellisen, R. Langer, A. Khademhosseini, Bioprinting the cancer microenvironment, ACS Biomater. Sci. Eng. 2 (10) (2016) 1710–1721.

[36] X. Zhou, et al., 3D bioprinting a cell-laden bone matrix for breast cancer metastasis study, ACS Appl. Mater. Interfaces 8 (44) (2016) 30017–30026.

[37] M. Cuvellier, et al., 3D culture of HepaRG cells in GelMa and its application to bioprinting of a multicellular hepatic model, Biomaterials 269 (2021), 120611.

[38] L. Antonioli, C. Blandizzi, P. Pacher, M. Guilliams, G. Haskó, Rethinking communication in the immune system: the quorum sensing concept, Trends Immunol. 40 (2) (2019) 88–97.

[39] I.F. Amado, et al., IL-2 coordinates IL-2–producing and regulatory T cell interplay, J. Exp. Med. 210 (12) (2013) 2707–2720.

[40] A.R. Almeida, et al., Quorum-sensing in CD4+ T cell homeostasis: a hypothesis and a model, Front. Immunol. 3 (2012) 125.

[41] C.A. Klebanoff, et al., Memory T cell–driven differentiation of naive cells impairs adoptive immunotherapy, J. Clin. Invest. 126 (1) (2016) 318–334.

[42] M.F. Elshal, J.P. McCoy, Multiplex bead array assays: performance evaluation and comparison of sensitivity to ELISA, Methods 38 (4) (2006) 317–323.

[43] H. Clevers, COVID-19: organoids go viral, Nat. Rev. Mol. Cell Biol. (2020) 1–2.

[44] M.A. Heinrich, R. Bansal, T. Lammers, Y.S. Zhang, R. Michel Schiffelers, J. Prakash, 3D-Bioprinted mini-brain: a glioblastoma model to study cellular interactions and therapeutics, Adv. Mater. 31 (14) (2019), 1806590.

[45] K.K. Dijkstra, et al., Generation of tumor-reactive T cells by co-culture of peripheral blood lymphocytes and tumor organoids, Cell 174 (6) (2018) 1586–1598, e12.

[46] K. Haskins, M. Portas, B. Bergman, K. Lafferty, B. Bradley, Pancreatic islet-specific T-cell clones from nonobese diabetic mice, Proc. Natl. Acad. Sci. USA 86 (20) (1989) 8000–8004.

[47] B. Lozanoska-Ochser, N.J. Klein, G.C. Huang, R.A. Alvarez, M. Peakman, Expression of CD86 on human islet endothelial cells facilitates T cell adhesion and migration, J. Immunol. 181 (9) (2008) 6109–6116.

[48] A.C. Luca, et al., Impact of the 3D microenvironment on phenotype, gene expression, and EGFR inhibition of colorectal cancer cell lines, PLoS One 8 (3) (2013), e59689.

[49] M.J. Barron, C.-J. Tsai, S.W. Donahue, Mechanical stimulation mediates gene expression in MC3T3 osteoblastic cells differently in 2D and 3D environments, J. Biomech. Eng. 132 (4) (2010).

[50] D. Huh, G.A. Hamilton, D.E. Ingber, From 3D cell culture to organs-on-chips, Trends Cell Biol. 21 (12) (2011) 745–754.